

# Simulating spectroscopic detection of Majorana zero modes with a superconducting quantum computer

John P. T. Stenger,<sup>1</sup> Gilad Ben-Shach,<sup>2</sup> David Pekker,<sup>3</sup> and Nicholas T. Bronn<sup>4</sup>

<sup>1</sup>*NRC Postdoctoral Associate, U.S. Naval Research Laboratory, Washington, DC 20375, United States*

<sup>2</sup>*IBM Quantum, IBM Canada, Markham, Ontario, L6G 1C7, Canada*

<sup>3</sup>*Department of Physics and Astronomy, University of Pittsburgh, Pittsburgh, PA 15260, USA*

<sup>4</sup>*IBM Quantum, IBM T.J. Watson Research Center, Yorktown Heights, New York 10598, USA*

We detect the remnants of the topological phase boundary of a two site Kitaev chain with Coulomb interactions using a spectroscopic eigensolver algorithm on a quantum computer. Along the boundary, even- and odd-parity states are degenerate and Majorana zero modes become spatially separated. The spectroscopic eigensolver interacts with a quantum register which simulates the evolution of the Hamiltonian system via an auxiliary “probe” qubit. The probe qubit is weakly coupled to the system so that it responds to the resonant transitions of the system.

The simulation of quantum systems with a quantum computer was originally proposed by Feynman [1] which sparked the nascent field. While the dynamics of quantum systems are fully determined (e.g. by the Schrödinger equation), the dimension of the Hilbert space that describes their evolution scales exponentially in the number of degrees of freedom which makes classical calculations impossible for a large enough system size. Computational methods such as mean field theory, density functional theory, and the density matrix renormalization group (to name a few) make approximations to quantum systems with some success, however, they tend to fail when the system under study has a large degree of entanglement, such as high-temperature superconductivity [2] and intrinsic (not symmetry protected) topological phases of materials [3, 4]. The recent availability of quantum computers on the cloud allows practitioners to begin to map problems of quantum simulation and achieve proof-of-principle results [5–7]. Some such demonstrations are even starting to surpass the accuracy of state-of-the-art classical approximations [8].

A major goal of the field of quantum simulation is to ascertain the eigenvalues of a system undergoing Hamiltonian evolution. Quantum computers may theoretically give an exponential speed-up to this problem by the celebrated quantum phase estimation (QPE) algorithm [9] – the backbone of proposed universal quantum simulation [10]. QPE estimates the phase of a unitary operator  $U$  acting on an  $n$ -dimensional Hilbert space encoded by a “simulation” register to within an arbitrary precision specified by the number  $m$  of qubits in an auxiliary register. Performing QPE involves realizing controlled- $U^k$  gates on  $n$  qubits (with  $1 \leq k \leq 2^{m-1}$ ) followed by an inverse quantum Fourier transform on the auxiliary register (as depicted in Fig. 1a), and is prohibitive for near-term noisy quantum hardware [11]. Current research thrusts for reducing the resources necessary for quantum simulation include replacing the  $m$ -qubit auxiliary register with a recycled “pointer” qubit via mid-circuit measurements and feed-forward known as iterative phase estimation [12] and repeatedly performing a single controlled- $U$  on the simulation register followed

by auxiliary qubit measurements to ascertain the phase from a classical Fourier transform of these expectation values [13]. Other methods propose interacting auxiliary qubits with a simulated system to elucidate its properties [14, 15]. Recently, algorithms such as the variational quantum eigensolver (VQE) have been used to find the eigenvalues of system Hamiltonians via repeated state preparation and measurement guided by a classical optimizer and the variational principle [16], which allows more flexibility for hardware-efficient solutions [17].

Here we propose a spectroscopic eigensolver method and use it to estimate the parity-inverting phase boundary in a two-site Kitaev chain with Coulomb interactions. Along this boundary, where even and odd parity states are degenerate, Majorana zero modes (MZMs) separate onto the two sites. This parity-inverting boundary is the precursor to the topological phase boundary in longer chains. Our method is akin to the experimental tool of tunneling spectroscopy, whereby the properties of a system are observed by its response as a function of probe energy. In this case, the probe qubit evolves as a function of energy (via  $\omega$ ) and interacts with a system that has undergone Hamiltonian evolution for a time  $t$  over a number of interleaved steps, as shown in Fig. 1b. Subsequent measurement of the probe qubit reveals the spectrum of the evolved Hamiltonian via dips in the  $\langle Z_0 \rangle$  expectation value when probe energy is equal to a energy transition in the system. While similar to QPE in many respects, this technique yields benefits for implementations with near-term noisy quantum computers because the controlled-unitaries have been interchanged with uncontrolled time evolution and a probe-system interaction that requires only two-qubit gates, followed by a measurement of the single probe qubit. This conserves resources in both the complexity of implementing controlled-unitaries on current quantum computers and the simplicity of measuring the response of the single qubit.

Coupling the probe qubit to the simulation register provides the freedom to select the specific qubit being probed. It is only necessary that the wavefunction of the simulation register has strong weight on the specific qubit being probed. In particular, MZMs are end

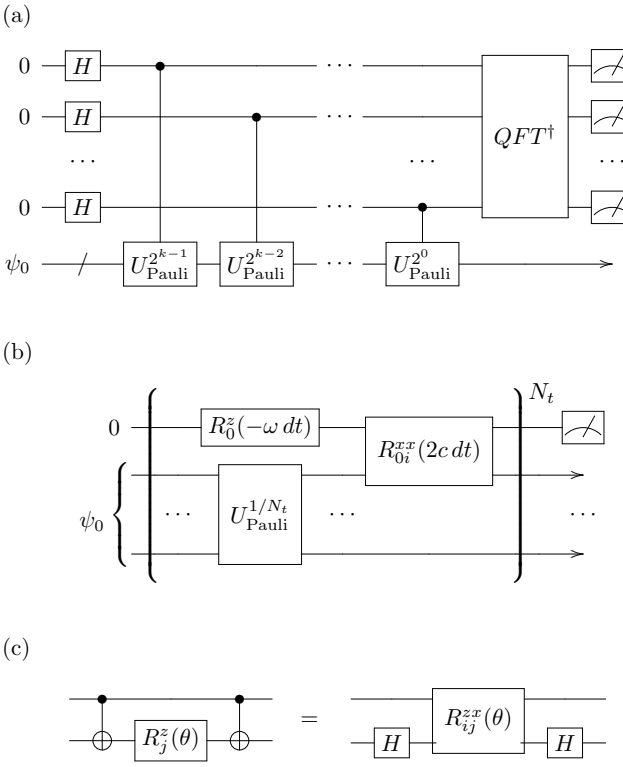


Figure 1. Quantum circuits for simulating the time evolution  $U_{\text{Pauli}} = e^{-iH_{\text{Pauli}}t}$ : (a) the QPE algorithm for an  $m$ -qubit auxiliary register interacting with an  $n$ -qubit simulation register with initial state  $|\psi_0\rangle$ , (b) the spectroscopic eigensolver algorithm for a probe qubit interacting with a single qubit of the  $n$ -qubit simulation register (for  $N_t$  first-order Trotter steps  $U_{\text{res}}$ ) followed by a single measurement, and (c) a circuit equivalence that allows the efficient implementation of scaled pulses with the native  $R^{zx}(\theta)$  interaction generated by echoed cross resonance [18], where  $\theta \sim V dt, \Delta dt, c dt$ , or  $\omega dt$ . Note that the Trotterization in (a) occurs inside each controlled- $U_{\text{Pauli}}$  whereas for (b) each Trotter step is repeated  $N_t$  times.

modes realized on an  $n$ -site Kitaev chain in the topological regime, and hence a perfect test case for the spectroscopic eigensolver technique discussed herein. Distinguishing the topological phase from the trivial superconducting phase in such nanowires has been a recent theoretical interest [19]. This interest is largely motivated by the fact that Majorana zero modes promise application in topologically protected quantum computation [20–24].

The model Hamiltonian of the interacting Kitaev chain with Coulomb interactions is (taking  $\hbar \equiv 1$  throughout)

$$H_{\text{sys}} = \mu \sum_{i=1}^L c_i^\dagger c_i + g \sum_{i=1}^{L-1} (c_i^\dagger c_{i+1} + c_{i+1}^\dagger c_i) + \Delta \sum_{i=1}^{L-1} (c_i^\dagger c_{i+1}^\dagger + c_{i+1} c_i) + V \sum_{i=1}^{L-1} c_i^\dagger c_i c_{i+1}^\dagger c_{i+1} \quad (1)$$

where  $L$  is the number of sites,  $c_i^\dagger$  ( $c_i$ ) is the creation (annihilation) operator on site  $i$ ,  $\mu$  is the chemical potential,  $g$  is the hopping rate,  $\Delta$  controls the superconductivity pairing strength, and  $V$  is the interaction strength. The inclusion of the interaction term makes the system difficult to study classically but poses no additional fundamental challenges for quantum processors [25, 26].

Using the Jordan-Wigner encoding [27], we can express Eq. 1 as

$$H_{\text{Pauli}} = x \sum_{i=1}^{n-1} X_i X_{i+1} + y \sum_{i=1}^{n-1} Y_i Y_{i+1} + z \sum_{i=1}^{n-1} Z_i Z_{i+1} - m \sum_{i=1}^n Z_i - \bar{m} \sum_{i=2}^{n-1} Z_i \quad (2)$$

where  $X_i, Y_i, Z_i$  are Pauli matrices acting on qubit  $i$ ,  $n = L$  is the number of qubits used to represent the system, and

$$x = \frac{g + \Delta}{2}, \quad y = \frac{g - \Delta}{2}, \quad z = \frac{V}{4} \\ m = \frac{2\mu + V}{4}, \quad \bar{m} = \frac{V}{4}. \quad (3)$$

In the limit  $L \rightarrow \infty$ , this system has a topological phase transition in parameter space. In the topological regime, the first excited state is degenerate with the ground state.

We can approach the  $L \rightarrow \infty$  limit by increasing the number of sites. In Fig. 2 we plot maps of the energy gap for different values of  $L$ . The parameters are set to  $x = 1.5$ ,  $z = \bar{m} = 0.4$ . The parameters are considered to be unitless algorithmic quantities, however, the values roughly correspond to those of real systems if they are taken to be in the meV range [28]. For  $L > 2$ , we see that the gap opens and closes multiple times. The larger  $L$  the more the gap closes and the smaller are the peaks between the lines where the gap closes. In this way, one could approach the case where the gap stays closed. From here on, we will restrict ourselves to the two-site  $L = 2$  model (results for the three-site model may be found in the Supplemental Material). In this case the gap between the ground and first excited state (i.e., the lowest even and lowest odd parity states) closes along the surface

$$m = \sqrt{z^2 + z(x+y) + xy} \quad (4)$$

This surface can be thought of as a remnant of the topological phase boundary. As the length of the system increases, the gap inside this surface will go to zero and will become a topological phase. We now explore the use of the novel spectroscopic eigensolver technique to analyze this surface.

The spectroscopic eigensolver technique finds the energy differences of a system by coupling a probe qubit to a Pauli Hamiltonian  $H_{\text{Pauli}}$  suitably encoded to enforce (anti-)commutation relations so that it represents a (fermionic) bosonic system Hamiltonian  $H_{\text{sys}}$ . The full

Hamiltonian, which we will refer to as the “resonance” Hamiltonian because of its response when the probe and system are on-resonance, is

$$H_{\text{res}} = -\frac{1}{2}\omega Z_0 + cX_0X_i + H_{\text{Pauli}}, \quad (5)$$

where the probe qubit  $q_0$  with energy  $\omega$  is at index 0,  $c$  is the coupling parameter between the probe and probed qubit  $q_i$  of the simulated system, and the tensor products with identity matrices are omitted for succinctness (we will focus on the Kitaev chain for which  $H_{\text{Pauli}}$  is given by Eq. (2)). If the time step  $dt$  is small, the first-order Suzuki-Trotter decomposition of the time evolution unitary is

$$U_{\text{res}}(\omega, dt) = e^{-iH_{\text{res}}dt} \approx R_{0i}^{xx}(2c dt) R_0^z(-\omega dt) U_{\text{Pauli}}^{1/N_t}, \quad (6)$$

where  $R_j^z(\phi)$  is a  $Z$ -rotation on site  $j$  and  $R_{jk}^{xx}(\theta)$  is an  $XX$ -rotation on sites  $j$  and  $k$ . Fig. 1b depicts a single Trotter step  $U_{\text{res}}$  (time evolution of  $dt$ ) whereas  $U_{\text{Pauli}} = e^{-iH_{\text{Pauli}}t}$  indicates the Trotterization for the entire time evolution  $t = N_t dt$ .

After  $N_t$  applications of  $U_{\text{res}}$ , we measure the probe qubit in the  $Z$ -basis,

$$\langle Z_0 \rangle(\omega) = 1 - 2 \sum_s |\langle 1, n | U_{\text{res}}(\omega)^{N_t} | 0, \psi_0 \rangle|^2, \quad (7)$$

where  $|0, \psi_0\rangle$  is the initial state of the qubits for which the probe qubit is in the ground state but all other qubits are arbitrarily prepared and  $|1, n\rangle$  represents a state for which the probe qubit is in the excited state and  $n \in \{n\}$  is a full representation of the system qubits. For simplicity we take  $|\psi_0\rangle$  to be the  $n$ -qubit ground state. When  $c$  is small compared to the energy scales in  $H_{\text{Pauli}}$  and when  $\omega$  is on resonance with an energy transition of  $H_{\text{Pauli}}$ , the probability of the probe qubit flipping will peak, resulting in a dip in  $\langle Z_0 \rangle(\omega)$ .

The following experiments were conducted within the Qiskit [29] framework with jobs sent to the cloud-based *ibm\_lagos*, a 7-qubit superconducting IBM Quantum backend. First, the Kitaev model Hamiltonian of Eq. 1 is represented as a fermionic operator and subsequently mapped to a Pauli Hamiltonian via a Jordan-Wigner decomposition. The Pauli Hamiltonian is then mapped to unitary time evolution via the second-order Suzuki-Trotter transformation. The resulting circuit consists of two-qubit rotations on the order of  $V dt, \Delta dt, c dt$ , and  $\omega dt$ , where the digital synthesis of each is locally equivalent to a  $Z$ -rotation sandwiched by two CNOTs, which is more efficiently implemented by scaled gates that rotate smaller angles in the two-qubit Hilbert space natively (the equivalence of which is shown in Fig. 1c) instead of the (net) two-qubit  $\pi$  rotation in the former case [5]. These scaled pulses are implemented as calibrations for  $R^{xx}(\theta)$  gates following an analysis of the circuit using a novel template optimization technique [30]. Each spectroscopic experiment is then built as an array of circuits,

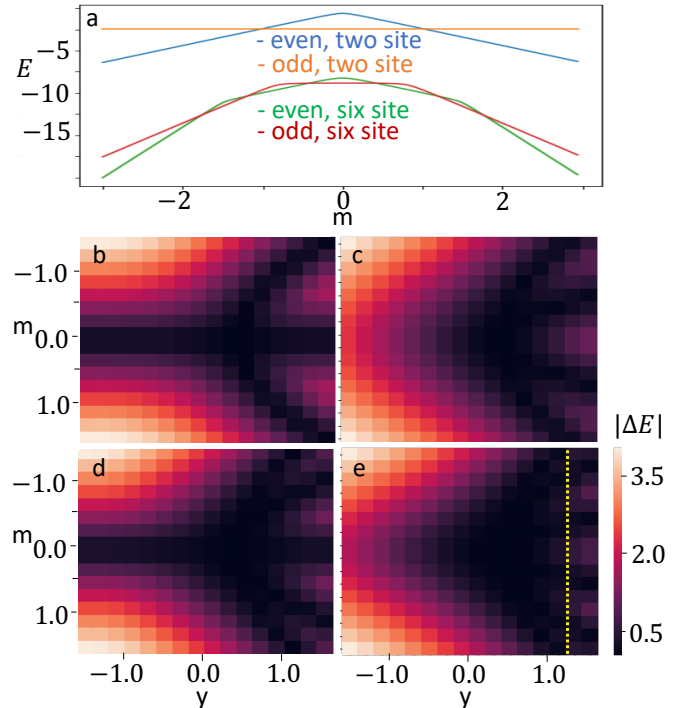


Figure 2. Energy gap for increasing chain length. The plots are generated from a classical simulation. In panel (a) we plot the (absolute) energy of the lowest even and lowest odd parity states versus  $m$  for two sites and for six sites at  $y = 1.3$  ( $m$  and  $y$  are defined in Eq. (4)). In the other panels, the energy gap between the lowest even and lowest odd parity state is plotted against the parameters  $m$  and  $y$ . The points where  $|\Delta E|$  goes to zero corresponds to the crossing of the two lowest energy levels. Each plot has a different number of sites: (b) three sites, (c) four sites, (d) five sites, (e) six sites, the dotted yellow line shows the location ( $y = 1.3$ ) of the six site energy cuts in panel (a). For a plot of the simulated 2-site model, see Fig. 4a.

one for each value of  $\omega$ . For each circuit, a result consisting of the measurement strings of 8192 shots is returned and analyzed. This allows us to find the energy transitions by locating dips in  $\langle Z_0 \rangle(\omega)$ . Further details are provided in the Supplementary Material and full data and source code can be found at [www.github.com/qiskit-research/mzm-phase-boundary](https://www.github.com/qiskit-research/mzm-phase-boundary).

We first optimized the time  $t$ , time step  $dt$  and coupling  $c$  so that the most accurate data could be collected (see Supplementary Material). In Fig. 3a we show a sweep of the probe qubit’s energy  $\omega$  for three values of  $c$ . The energy difference between the ground and first excited state is determined by the  $\omega$  at which  $\langle Z_0 \rangle(\omega)$  is minimum. When  $c$  is too low, the probe qubit will not respond to the system but if  $c$  is too high it will perturb the system. Once the optimum  $c$  value was found we optimized time step  $dt$  and total time  $t$  in a similar way. Then we re-optimized  $c$  at the new values of  $t$  and  $dt$  and found

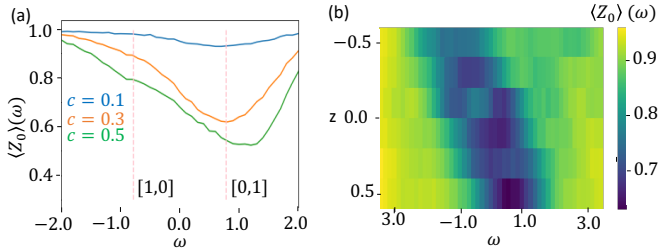


Figure 3. Sweeps of the probe qubit frequency. (a) optimization of the  $c$  parameter. For these sweeps,  $m = 1.0$ ,  $x = 1.5$ ,  $y = 0.4$ ,  $z = 0.2$ . The vertical lines are the expected transitions from the classical solution. For a more  $c$ -sweeps see the Supplemental Material. (b) Sweeps of  $\omega$  for several values of  $z$ . For these sweeps,  $c = 0.3$ ,  $m = 1.0$ ,  $x = 1.5$ , and  $y = 0.7$ . For both plots,  $dt = 0.7$  and  $t = 5$ .

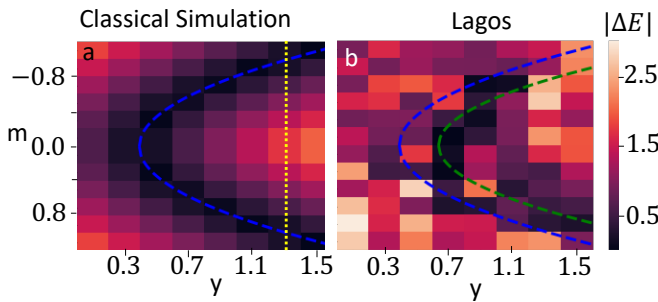


Figure 4. Energy difference between the ground and first excited state as a function of  $m$  and  $y$ . (a) Simulation on a classical computer with no error. The dotted yellow line shows the location ( $y = 1.3$ ) of the two site energy cuts plotted in Fig. 2a, (b) results from the *ibm\_lagos* backend. In both plots,  $c = 0.3$ ,  $x = 1.5$ ,  $z = -0.4$ ,  $dt = 0.7$ , and  $t = 5.0$ . The blue curve in both plots is the expected zero-crossing from Eq. 4 with the above parameters. The green curve in (b) is the zero-crossing shifted to  $z = -6.5$ .

that the optimum  $c$  value had not changed.

Note the state transition from ground to first excited (denoted by the notation  $[0,1]$ ) is visible in Fig. 3a but the reverse transition is not. This is due the initial state of the system qubits, set to  $|00\rangle$  for simplicity, which has no overlap with the odd parity excited state and so only the forward transition is possible. The reverse transition is determined by symmetry (the negative energy of the forward transition). Considering a single parity, in this way, allows maximum contrast in our signal. It is also beneficial to have as few transitions as possible within the energy range of interest to prevent smearing between the dips in  $\langle Z_0 \rangle$ . Fig. 3b displays the gap's dependence on interaction strength  $z$ . The value of the gap energy is located where the value of  $\langle Z_0 \rangle$  is minimum. We are interested in the points where the gap energy goes to zero, corresponding to the location of the parity-flipping phase boundary.

Taking several scans of  $\omega$  for different values of  $m$  and  $y$ , we are able to trace out the parity-flipping phase boundary. Fig. 4 shows the absolute value of the gap for (a) a classical simulation without noise and (b) the results from the quantum device. The points at which the gap goes to zero is the phase boundary. Notice that in the results from the quantum device the boundary is pushed to higher values of  $y$  than in the perfect simulation. We attribute this discrepancy to unintended  $ZZ$  rotations, a well-known error for quantum computers built from fixed-frequency transmons [31, 32]. A rough calculation from the static  $ZZ$  interactions of 140-150 kHz measured for the physical qubits [33] of *ibm\_lagos* yields a predicted difference  $\Delta z = 2.6$  between the curves in Fig. 4b, whereas the difference  $\Delta z = 6.1$  between the blue and green curves is plotted. This simple estimate neglects the effect of cross resonance-induced  $ZZ$  interactions [34], yet provides evidence of possible sources of error that may be suppressed by error mitigation techniques [8].

While the energy transitions are symmetric between positive and negative values of  $m$ , it is often the case that a particular transition is more apparent in the data for either positive or negative  $m$ . The issue is that at certain parameter values, the  $[2, 3]$  transition washes out the response from the  $[0, 1]$  transition. We find that the zero crossing of the  $[0, 1]$  transition is easily extractable from the data for negative  $m$  in the range of  $0.7 \leq y \leq 1.1$  while for  $1.1 < y$  the positive  $m$  values show the  $[0, 1]$  zero-crossing clearly. By applying symmetry in  $m$  we have a clear map of the zero-crossing in the full range of data that was taken. Further analyses of these parameter regimes are found in the Supplemental Material.

The experiments discussed here demonstrate the ability of the novel spectroscopic eigensolver technique to map the remnants of a boundary between the trivial superconducting and topological phases in an interacting two-site Kitaev chain. Similar to the experimental method of tunneling spectroscopy, the simulation register interacts with a local probe qubit to determine its spectrum. This requires only the realization of two-qubit interactions between the probe and register without the coherent control of the register at the heart of many other simulation algorithms, making this technique highly amenable to exploration on near-term noisy quantum computing hardware.

The authors acknowledge the use of IBM Quantum Services for this work. The authors also thank C.S. Hellberg, L.D. Gunlycke, D.J. Egger, S.M. Frolov, P. Jurcevic, and Y. Kim for insightful discussions, D.T. McClure, P. Nation, S. Panda and R. Woo for assistance in performing the experiments, and K.J. Ferris, O.T. Lanes, and K.J. Sung for careful readings of the manuscript. We acknowledge the Air Force Research Laboratory (AFRL) for providing additional quantum resources through its partnership with IBM.

---

[1] R. P. Feynman, *International Journal of Theoretical Physics* **21**, 467 (1982).

[2] C. C. Tsuei and J. R. Kirtley, *Reviews of Modern Physics* **72**, 969 (2000).

[3] M. Z. Hasan and C. Kane, *Reviews of Modern Physics* **82**, 3045 (2010).

[4] A. Bansil, H. Lin, and T. Das, *Reviews of Modern Physics* **88**, 021004 (2016).

[5] J. P. T. Stenger, N. T. Bronn, D. J. Egger, and D. Pekker, *Physical Review Research* **3**, 033171 (2021).

[6] X. Xiao, J. K. Freericks, and A. F. Kemper, *Quantum* **5** (2021).

[7] M. J. Rančić, [arXiv:2108.07235](https://arxiv.org/abs/2108.07235).

[8] Y. Kim, C. J. Wood, T. J. Yoder, S. T. Merkel, J. M. Gambetta, K. Temme, and A. Kandala, [arXiv:2108.09197](https://arxiv.org/abs/2108.09197).

[9] A. Y. Kitaev, [arXiv:9511026](https://arxiv.org/abs/9511026).

[10] S. Lloyd, *Science* **273**, 1073 (1996).

[11] J. Preskill, *Quantum* **2**, 79 (2018).

[12] A. D. Córcoles, M. Takita, K. Inoue, S. Lekuch, Z. K. Minev, J. M. Chow, and J. M. Gambetta, *Physical Review Letters* **127**, 100501 (2021).

[13] R. D. Somma, *New Journal of Physics* **21**, 123025 (2019).

[14] H. Wang, S. Ashhab, and F. Nori, *Physical Review A* **85**, 062304 (2012).

[15] B. M. Terhal and D. P. DiVincenzo, *Physical Review A* **61**, 22 (2000).

[16] A. Peruzzo, J. R. McClean, P. Shadbolt, M.-H. H. Yung, X.-Q. Q. Zhou, P. J. Love, A. Aspuru-Guzik, J. L. O’Brien, and J. L. O’Brien, *Nature Communications* **5**, 4213 (2014).

[17] A. Kandala, A. Mezzacapo, K. Temme, M. Takita, M. Brink, J. M. Chow, and J. M. Gambetta, *Nature* **549**, 242 (2017).

[18] S. Sheldon, E. Magesan, J. M. Chow, and J. M. Gambetta, *Physical Review A* **93**, 060302 (2016).

[19] G. Ben-Shach, A. Haim, I. Appelbaum, Y. Oreg, A. Yacoby, and B. I. Halperin, *Physical Review B* **91**, 045403 (2015).

[20] A. Y. Kitaev, *Annals of Physics* **303**, 2 (2003).

[21] C. Nayak, S. H. Simon, A. Stern, M. Freedman, and S. S. Das Sarma, *Reviews of Modern Physics* **80**, 1083 (2008).

[22] J. Alicea, Y. Oreg, G. Refael, F. von Oppen, and M. P. A. Fisher, *Nature Physics* **7**, 412 (2011).

[23] P. Bonderson and R. M. Lutchyn, *Physical Review Letters* **106**, 130505 (2011).

[24] J. P. T. Stenger, M. Hatridge, S. M. Frolov, and D. Pekker, *Physical Review B* **99**, 035307 (2019).

[25] A. M. Childs, D. Maslov, Y. Nam, N. J. Ross, and Y. Su, *Proceedings of the National Academy of Sciences of the United States of America* **115**, 9456 (2018).

[26] F. Tacchino, A. Chiesa, S. Carretta, and D. Gerace, *Advanced Quantum Technologies* **3**, 1900052 (2020).

[27] R. Somma, G. Ortiz, J. E. Gubernatis, E. Knill, and R. Laflamme, *Physical Review A* **65**, 042323 (2002).

[28] J. Chen, P. Yu, J. Stenger, M. Hocevar, D. Car, S. R. Plissard, E. P. A. M. Bakkers, T. D. Stanescu, and S. M. Frolov, *Science Advances* **3** (2017), 10.1126/sci-adv.1701476.

[29] “Qiskit: An open-source framework for quantum computing,” (2021).

[30] R. Iten, R. Moyard, T. Metger, D. Sutter, and S. Woerner, [arXiv:1909.05270](https://arxiv.org/abs/1909.05270).

[31] A. Kandala, K. X. Wei, S. Srinivasan, E. Magesan, S. Carnevale, G. A. Keefe, D. Klaus, O. Dial, and D. C. McKay, *Physical Review Letters* **127**, 130501 (2020).

[32] N. Sundaresan, I. Lauer, E. Pritchett, E. Magesan, P. Jurcevic, and J. M. Gambetta, *PRX Quantum* **1**, 020318 (2020).

[33] K. X. Wei, E. Magesan, I. Lauer, S. Srinivasan, D. F. Bogorin, S. Carnevale, G. A. Keefe, Y. Kim, D. Klaus, W. Landers, N. M. Sundaresan, C. Wang, E. J. Zhang, M. Steffen, O. E. Dial, D. C. McKay, and A. Kandala, [arXiv:2106.00675](https://arxiv.org/abs/2106.00675).

[34] M. Takita, A. D. Córcoles, E. Magesan, B. Abdo, M. Brink, A. W. Cross, J. M. Chow, and J. M. Gambetta, *Physical Review Letters* **117**, 210505 (2016).

[35] P. Roushan, C. Neill, J. Tangpanitanon, V. M. Bastidas, A. Megrant, R. Barends, Y. Chen, Z. Chen, B. Chiaro, A. Dunsworth, A. Fowler, B. Foxen, M. Giustina, E. Jeffrey, J. Kelly, E. Lucero, J. Mutus, M. Neeley, C. Quintana, D. Sank, A. Vainsencher, J. Wenner, T. White, H. Neven, D. G. Angelakis, and J. Martinis, *Science* **358**, 1175 (2017).

---

## I. FUNCTIONAL FORM OF THE RESONANCE EIGENSOLVER

The algorithm works by applying unitary time evolution to an arbitrary state (in our simulation we choose  $|\psi_0\rangle = |00\rangle$ ) of the system with the probe qubit in the ground state. We then observe the probability that the probe qubit becomes excited. If the energy on probe qubit (as swept by  $\omega$  in the resonance Hamiltonian, not the actual transition energy of transmon as in [35]) matches an energy transition in the system then we will find a peak in the probability. To demonstrate that the probability indeed peaks at energy transitions we will use two approaches. First we will derive the first order perturbation of the probability as a function of probe qubit frequency. This will show us that the probability decays as the frequency of the probe qubit is taken off resonance. Second we will analyze the behavior of the probability when the system is composed of only two energy levels. Since the probability decays away from resonance, a two level system is a good approximation for a larger system where a particular transition is close to resonance with the probe qubit.

Let us start with the perturbation approach. In the algorithm, we apply unitary time evolution

$$U_{\text{res}}(\omega) = e^{-i(-\omega Z_0/2 + H_{\text{Pauli}} + c X_0 X_i)dt} \quad (8)$$

where  $H_{\text{Pauli}}$  is the qubit-encoded system Hamiltonian, qubit zero is the probe qubit, and qubit  $i$  is the qubit being probed. We desire  $c$  to be small so that we can treat the  $c X_0 X_i$  term as a perturbation. Let  $E_n$  and  $|n\rangle$  be the energies and eigenvectors of the system Hamiltonian  $H_{\text{Pauli}}$   $|n\rangle = E_n |n\rangle$  so that the unperturbed eigenvalues are  $E_{a,n} = (-1)^{a+1} \omega/2 + E_n$  and the unperturbed eigenvectors are  $|a,n\rangle$  where  $a \in \{0, 1\}$  labels the state of the probe qubit, i.e.

$$\begin{aligned} \left(-\frac{1}{2}\omega Z_0 + H_{\text{Pauli}}\right) |a,n\rangle &= E_{a,n} |a,n\rangle \\ &= \left(\frac{(-1)^{a+1}}{2}\omega + E_n\right) |a,n\rangle. \end{aligned} \quad (9)$$

Let  $\bar{E}_{an}$  be the energy of the entire resonance Hamiltonian and  $|\bar{a}n\rangle$  be the eigenvectors so that

$$\left(-\frac{1}{2}\omega Z_0 + H_{\text{Pauli}} + c X_0 X_1\right) |\bar{a}n\rangle = \bar{E}_{an} |\bar{a}n\rangle \quad (10)$$

To first order in  $c$  we have,

$$\begin{aligned} \bar{E}_{an} &\approx E_{an} + c \langle a,n | X_0 X_1 | a,n \rangle = E_{an} \\ |\bar{a}n\rangle &\approx |a,n\rangle + c \sum_{bm \neq an} |bm\rangle \frac{\langle bm | X_0 X_1 | an \rangle}{E_{an} - E_{bm}}. \end{aligned} \quad (11)$$

The initial state of the algorithm has the probe qubit in the ground state and the system qubits in an arbitrary

state. We are interested in the probability that the auxiliary qubit will flip regardless of the state of the system after time evolution. We can write the entire algorithm in one line,

$$\langle Z_0 \rangle(\omega) = 1 - 2 \sum_m \left| \sum_n \alpha_n \langle 1m | U_{\text{res}}(\omega)^{N_t} | 0n \rangle \right|^2 \quad (12)$$

where the parameters  $\alpha_n$  are arbitrary reflecting that we start in an arbitrary state of the system. To evaluate this probability, we need to evaluate

$$\begin{aligned} \langle 1m | \left(-\frac{1}{2}\omega Z_0 + H_S + c X_0 X_1\right)^l | 0n \rangle = \\ \sum_{ak} \langle 1m | \bar{a}k \rangle \langle \bar{a}k | 0n \rangle \bar{E}_{ak}^l \end{aligned} \quad (13)$$

where  $l$  is any non-negative integer. To first order, we have

$$\langle 1m | \bar{a}k \rangle = \delta_{a1} \delta_{km} + c \frac{\chi_{mk}}{E_{0m} - E_{1k}} \delta_{a0} \quad (14)$$

$$\langle \bar{a}k | 0n \rangle = \delta_{a0} \delta_{kn} + c \frac{\chi_{kn}}{E_{1k} - E_{0n}} \delta_{a1} \quad (15)$$

where  $\chi_{mn} = \langle m | X_1 | n \rangle$ . We multiply these together and get,

$$\begin{aligned} \langle 1m | \left(-\frac{1}{2}\omega Z_0 + H_S + c X_0 X_1\right)^l | 0n \rangle = \\ c \chi_{mn} \left( \frac{E_{1m}^l}{E_{1m} - E_{0n}} + \frac{E_{0n}^l}{E_{0m} - E_{1n}} \right). \end{aligned} \quad (16)$$

Now we can go back to the probability

$$\begin{aligned} \langle Z_0 \rangle(\omega) = \\ 1 - 2c^2 \left| \sum_{mn} \alpha_n \chi_{mn} \left( \frac{e^{iE_{1m}t}}{E_m - E_n + \omega} + \frac{e^{iE_{0n}t}}{E_m - E_n - \omega} \right) \right|^2 \end{aligned} \quad (17)$$

We see that the biggest contributions to the probability are the energies which are on resonance with the probe qubit. The pole at  $\omega = \pm(E_m - E_n)$  is unphysical since the perturbation is only valid for  $c < E_m - E_n - \omega$  for all  $m$  and  $n$ .

To analyze the behavior near the resonance condition  $\omega = \pm(E_1 - E_0)$ , we can ignore the other energy levels since they do not contribute as strongly. In this case we are left with a two level system. We can fully analytically analyze our algorithm for this two level system which will tell us generally the behaviour of the algorithm when  $\omega$  is near an energy transition. Let us write the two level system Hamiltonian as,

$$H_0 = \frac{1}{2} dZ_1 \quad (18)$$

where  $d = E_1 - E_0$ . The full Hamiltonian is,

$$H = \frac{1}{2}\omega Z_0 + \frac{1}{2}dZ_1 + cX_0X_1 \quad (19)$$

This has eigenvalues

$$\begin{aligned} E_a^\pm &= \pm\frac{1}{2}\sqrt{4c^2 + (d - \omega)^2} \\ E_b^\pm &= \pm\frac{1}{2}\sqrt{4c^2 + (d + \omega)^2} \end{aligned} \quad (20)$$

and eigenvectors

$$\begin{aligned} |a\pm\rangle &= \left( \frac{d - \omega + 2E_a^\pm}{2N_a^\pm} |01\rangle - \frac{c}{N_a^\pm} |10\rangle \right) \\ |b\pm\rangle &= \left( \frac{d + \omega + 2E_b^\pm}{2N_b^\pm} |00\rangle + \frac{c}{N_b^\pm} |11\rangle \right) \end{aligned} \quad (21)$$

where

$$\begin{aligned} N_a^\pm &= \frac{1}{\sqrt{2}}\sqrt{(d - \omega)^2 + 4c^2 - 2(d - \omega)E_a^\pm} \\ N_b^\pm &= \frac{1}{\sqrt{2}}\sqrt{(d + \omega)^2 + 4c^2 + 2(d + \omega)E_b^\pm} \end{aligned} \quad (22)$$

Thus, we can write time evolution as,

$$e^{-iHt} = e^{-iE_a^-}|a-\rangle\langle a-| + e^{-iE_a^+}|a+\rangle\langle a+| + e^{-iE_b^-}|b-\rangle\langle b-| + e^{-iE_b^+}|b+\rangle\langle b+| \quad (23)$$

Using this form of the time evolution operator it is straight forward (although tedious) to derive the bracket,

$$\langle 1m|e^{iH(\omega)t}|0n\rangle = A(\omega)\delta_{n1}\delta_{m0} + B(\omega)\delta_{n0}\delta_{m1} \quad (24)$$

where

$$\begin{aligned} A(\omega, d) &= i\frac{2c}{\sqrt{4c^2 + (d - \omega)^2}} \sin(E_a t) \\ B(\omega, d) &= i\frac{2c}{\sqrt{4c^2 + (d + \omega)^2}} \sin(E_b t) \end{aligned} \quad (25)$$

Once again, we see that the probability is maximized when  $\omega = \pm d$ .

We use the functional form to assist in finding the minima in the data. Figure 5 shows the functional form fitted to the data from *ibm\_lagos*. We begin the fitting by smoothing the data (averaging over the nearest four data points) and then finding the zeros in the derivative. We expect two energy transitions within the data range, specifically the  $[0,1]$  transition and the  $[2,3]$  transition which are both small. If we find two zeros (left panel in Fig. 5)) then we take the ten nearest points to each minimum found by the derivative and separately fit them to  $|A(\omega, d)|^2$ . If we find only one minimum (right panel in Fig. 5)) then we take the 20 nearest points and fit it to  $|A(\omega, d1) + A(\omega, d2)|^2$ . In other words, we expect that the two transitions are close enough that they form a single dip.

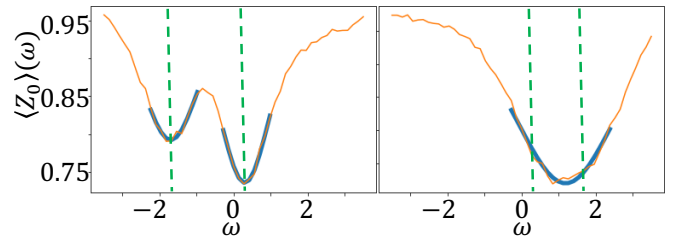


Figure 5. Fit of the *ibm\_lagos* data to the functional form. The orange curves are the experimental data, the blue curves are the fit, and the green dashed lines show the location of the transitions according to the fit.

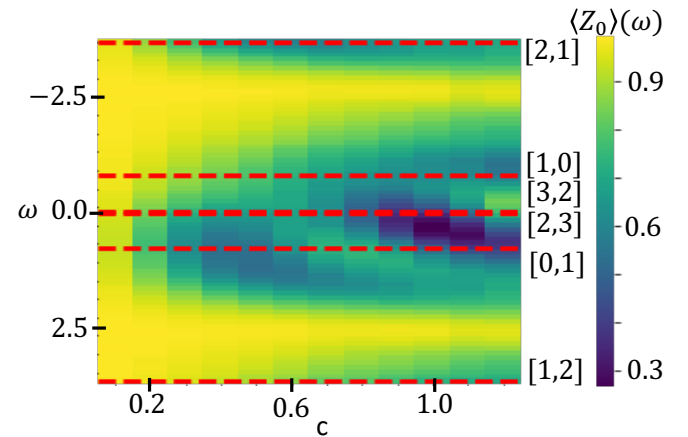


Figure 6. Expectation values of the  $Z$ -component of the probe qubit as a function of  $\omega$  and  $c$ . The other parameters are set to  $x = 1.5$ ,  $y = 0.4$ ,  $z = -0.3$ ,  $t = 5.0$ ,  $dt = 1.2$ . The dashed red lines show the location of the energy transitions. The lines are labeled on the right of the figure by the two states involved in the transition, e.g.  $[0, 1]$  is the transition from state 0 to state 1.

## II. OPTIMIZATION

The coupling strength  $c$  between the probe qubit and the system, the total evolution time  $t$ , and the time step  $dt$  all need to be optimized for the algorithm. In Fig. 6 we see the orientation of the probe qubit as a function of both  $\omega$  and  $c$ . We want to focus on the ground to first excited state transition labeled  $[0, 1]$  in the figure. We see that when  $c > 0.5$  the dip corresponding to the  $[0, 1]$  transition is shifted due to the large interaction between the probe and the system, and in fact the reverse transition  $[1, 0]$  and higher-order transitions  $[2, 3]$  and  $[3, 2]$  also appear (yet also shifted) at these strong coupling values. However, for  $c < 0.1$  the dip is washed out. We choose  $c = 0.3$  where the dip corresponding to the correct transition ( $[0, 1]$ ) is apparent and at the correct value, and no other nearby transitions are observed.

Figure 7 shows the  $Z$ -expectation of the probe qubit as a function of  $\omega$  and  $t$  for two values of  $dt$ . We see that

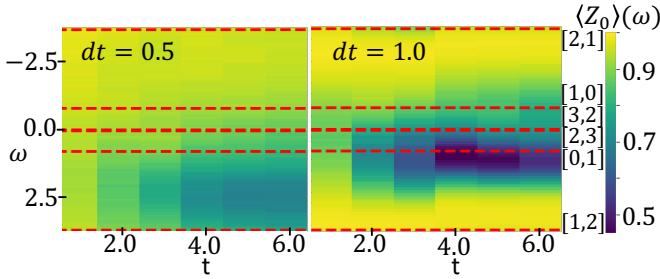


Figure 7. Expectation values of the  $Z$ -component of the probe qubit as a function of  $\omega$  and  $t$  for  $dt = 0.5$  (left) and  $dt = 1.0$  (right). The other parameters are set to  $x = 1.5$ ,  $y = 0.4$ ,  $z = -0.3$ ,  $t = 0.4$ . The dashed red lines show the location of the energy transitions. The lines are labeled on the right of the figure by the two states involved in the transition, e.g.  $[0, 1]$  is the transition from state 0 to state 1.

if  $t$  is too short the dip is washed out just like for small  $c$ . Additionally, if  $dt$  is too small then we run into errors due to the increased number of gates that are applied to the quantum register. We want the smallest  $dt$  we can manage so that our Suzuki-Trotter decomposition is as accurate as possible.

Informed by these optimization experiments and others, we chose the parameter set  $t = 5.0$ ,  $dt = 0.7$ ,  $c = 0.3$  for this work. More data was analyzed than those presented here, and we have made our full data set accessible at [www.github.com/qiskit-research/mzm-phase-boundary](https://www.github.com/qiskit-research/mzm-phase-boundary).

### III. APPLYING THE CHEMICAL POTENTIAL SYMMETRY

We know that the energy spectrum is symmetric about  $m \rightarrow -m$ . Therefore, if we know the zero-crossing phase boundary for  $+m$  we can infer the phase boundary for  $-m$  and visa-versa. Figure 8 shows the energy gap as a function of  $m$  and  $y$ . Here we selected the smallest gap between positive and negative  $m$  to be the gap for both. The justification for removing the higher gap values is that sometimes the  $[2, 3]$  transition has a much larger response than the  $[0, 1]$  transition. When this happens the  $[2, 3]$  transition can wash out the  $[0, 1]$  transition so that the fitting technique fails to provide an accurate estimate of the  $[0, 1]$  transition. Thus we get more accurate data by selecting between the transitions at positive and negative  $m$ .

### IV. THREE SITE MODEL DATA

We ran the spectroscopic algorithm for a three site Kitaev chain. While the data is very accurate at certain parameter values, we were not able to map out the full

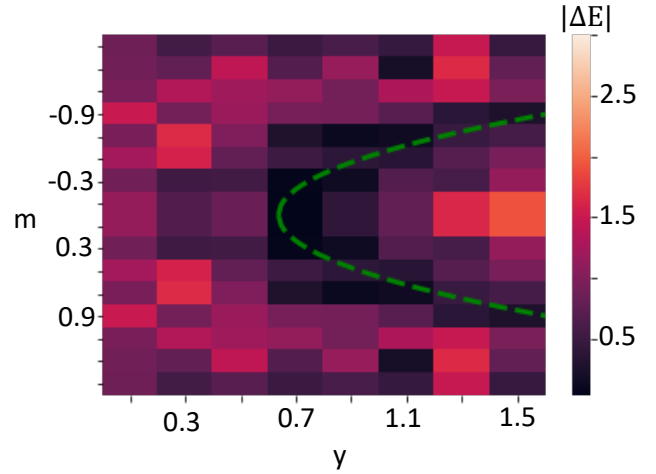


Figure 8. Energy gap as a function of  $m$  and  $y$  made to be symmetric across  $m = 0$ . The parameter values match those in Fig. 4 of the main text. The dashed curve is calculated from Eq. (4) of the main text using the same shift as in Fig 4.

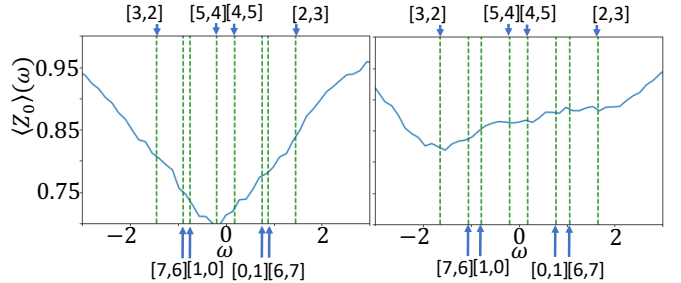


Figure 9. Expectation of the  $Z$ -component of the probe qubit as a function of  $\omega$  for a three-site Kitaev chain. Left: for  $m = 0.5$ . Right: for  $m = -0.5$ . The other parameters are set to  $x = 1.5$ ,  $y = 1.1$ ,  $z = 0.4$ ,  $c = 0.3$ ,  $dt = 0.7$ ,  $t = 5$ . The green dashed lines show the energy transitions which are labeled at the top/bottom of the plot.

phase diagram. One issue is that the number of small-energy transitions increases causing the width of the dips in  $\langle Z_0 \rangle(\omega)$  to often absorb several of the weaker transitions. In Fig. 9 we plot  $\langle Z_0 \rangle(\omega)$  for  $m = 0.5$  (left) and  $m = -0.5$  (right). While the energy transitions are symmetric in  $m$ , the algorithm often favors different transitions for positive and negative  $m$ . In this case, the  $[5, 4]$  transition is favored for positive  $m$  while  $[3, 2]$  is favored for negative  $m$ . While this asymmetry in the favored transition is present for the two site case as well, there we were able to resolve the secondary transition for many parameter values. For the three site model, the secondary transitions are very difficult to resolve if they are present at all.

Still, we are able to trace out the zero crossings for

certain energy transitions for a range of parameters. Figure 10 shows the zero-crossing for the  $[5, 4]$  transition in a small range of  $m$  and  $y$ . While the transition is shifted just like in the two site case, the main features are present. The data could be improved by narrowing the dips in  $\langle Z_0 \rangle(\omega)$ . A possible solution for narrowing the dips would be to increase  $t$ , which for this current work was limited by qubit coherence and classical waveform generation bandwidth for *ibm\_lagos*. It is expected that future generations of superconducting quantum backends will allow for such exploration.

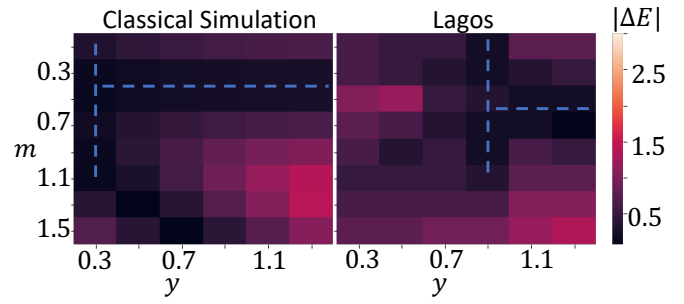


Figure 10. The  $[5, 4]$  energy transition as a function of  $y$  and  $m$ . Left: from directly solving for the eigenvalues of the Hamiltonian. Right: from the spectroscopic algorithm ran on Lagos. The other parameters are set to  $x = 1.5$ ,  $z = 0.4$ ,  $c = 0.3$ ,  $dt = 0.7$ ,  $t = 5$ .